ARTICLE

Fabrication of PdSe₂/GaAs Heterojunction for Sensitive Near-Infrared Photovoltaic Detector and Image Sensor Application

Lin-bao Luo[a]*, Xiu-xing Zhang[a], Chen Li[a], Jia-xiang Li[a], Xing-yuan Zhao[b], Zhi-xiang Zhang[a], Hong-yun Chen[a], Di Wu[c], Feng-xia Liang[b]*

a. School of Electronic Science and Applied Physics, Hefei University of Technology, Hefei 230009, China
b. School of Materials Sciences and Engineering, Hefei University of Technology, Hefei 230009, China
c. School of Physics and Microelectronics, Zhengzhou University, Zhengzhou 450052, China

In this study, we have developed a high-sensitivity, near-infrared photodetector (NIRPD) based on PdSe₂/GaAs heterojunction, which was made by transferring a multilayered PdSe₂ film onto a planar GaAs. The as-fabricated PdSe₂/GaAs heterojunction device exhibited obvious photovoltaic behavior to 808 nm illumination, indicating that the NIRPD can be used as a self-driven device without external power supply. Further device analysis showed that the hybrid heterojunction exhibited a high on/off ratio ratio of 1.16×10^5 measured at 808 nm under zero bias voltage. The responsivity and specific detectivity of photodetector were estimated to be 171.34 mA/W and 2.36×10^{11} Jones, respectively. Moreover, the device showed excellent stability and reliable repeatability. After 2 months, the photoelectric characteristics of the NIRPD hardly degrade in air, attributable to the good stability of the PdSe₂. Finally, the PdSe₂/GaAs-based heterojunction device can also function as a NIR light sensor.

Key words: van der Waals heterojunction, Two dimensional materials, NIR light photodetector, Image sensor, Responsivity

I. INTRODUCTION

High-performance and low-cost photonic detector is a kind of optoelectronic devices that can transform light signals to electrical ones. They have demonstrated a broad range of application in both modern technology and industry [1–3]. Compared with other photodetectors operating in visible light range, near-infrared (NIR, correspondingly to the electromagnetic radiation with typical wavelength ranging from 0.78 μm to 3.0 μm) devices have attracted significant research interest worldwide in the past several decade, due to their potential importance in military and civilian fields such as target detection, night vision, surveillance, security inspection, environmental monitoring, video and biomedical imaging, *etc.* [4–6]. Currently, the sensing of NIR light in the market is largely dominated by high-performance photodetectors made of crystalline silicon. Nonetheless, it should be noted that owing to its cut-off wavelength at about 1100 nm, the silicon NIR photodetectors are often characterized by relatively narrow wavelength photoresponse, which constitutes a bottleneck issue for their

practical application. Recently, people have resorted to other compound semiconductor materials such as InGaAs and GeSi alloy with tunable bandgap in NIR region to detect longer-wavelength infrared light [7–9]. In addition to InGaAs and GeSi, a variety of NIR photodetectors with different device geometries have been fabricated by using other narrow bandgap semiconductors (*e.g.*, HgCdTe, Ge, PbS, InSb) [10–13] and even topological insulators have been proposed [14]. Although these NIR photodetectors (NIRPD) with superior performance have been successfully achieved, it is undeniable that these devices still have their own shortcomings that cannot be ignored. For instance, the fabrication of these compounds usually involves the usage of very complicated growth instruments with expensive and complex manufacturing processes [15, 16]. Therefore, the development of simple, low-cost and highly efficient NIRPD still remains great challenges.

As a new material with unique atomic structure and excellent electrical and optoelectronic properties, two-dimensional (2D) layered material has also provided reliable solutions for the manufacture of various high-performance NIRPDs. For example, graphene is the earliest discovered 2D material with ultra-high mobility [17, 18]. It has been widely used for its excellent electrical properties, such as optoelectronic devices [19, 20], chemical biosensors [21, 22]. When combining metallic

---

*Authors to whom correspondence should be addressed. E-mail: luolb@hfut.edu.cn, fxliang@hfut.edu.cn

1

graphene with narrow bandgap semiconductors [23–26], the as-formed graphene-narrow bandgap semiconductor hybrid structures that are often characterized by strong built-in electric field at the interface will be an ideal building block for efficient NIR light detection. During the light detection process, the narrow band gap semiconductors are mainly used as light absorbing layers, and the photogenerated electron-hole pairs can be easily separated by the built-in electric field and then transported to separate electrodes. In spite of these extensive progress, it is undeniable that due to the lack of intrinsic band gap, the graphene in most of the hybrid structure NIRPD mainly acts as a transparent electrode material, which can hardly contribute to photoresponse in longer wavelength region. In light of this, some 2D materials with adjustable band gap have also been reported, including MoS_2 [27], WS_2 [28], $MoSe_2$ [29], $MoTe_2$ [30], *etc.* Very recently, 10 groups TMD palladium diselenide ($PdSe_2$) with superior optoelectronic properties, adjustable band gaps and stable crystal structure in the air have been discovered [31–33]. Its bandgap can be easily tailored from 1.1 eV of single layer to zero of multilayer [34]. With these advantages, it has been used for assembly of a variety of high-performance broadband PDs with different device configurations [35, 36].

Inspired by this, we herein report on the development of a high-performance hybrid heterojunction NIRPD made of planar GaAs wafer and multilayer $PdSe_2$, which was fabricated by a simple selenization approach. Device analysis found that the as-assembled $PdSe_2$/GaAs hybrid heterojunction displayed apparent photovoltaic behavior under 808 nm NIR light irradiation, with very good reproducibility and excellent ambient stability. What is more, the capability of the PdSe2/GaAs device for recording a simple NIR light image was also evaluated, which exhibited good potential in image sensor application.

II. EXPERIMENTS

A. Material preparation

The 2D $PdSe_2$ nanofilm was synthesized by a simple selenization method with CVD. In short, a ∼8 nm Pd film was firstly deposited onto a SiO_2/Si (300 nm SiO_2 thickness) substrate pre-cleaned by acetone, alcohol and deionized water using electron-beam evaporation. Then, the SiO_2/Si loaded with Pd-film was placed in the heating center area of the furnace. The selenium powder (99.99% purity) was placed in the center upstream area and Ar_2/H_2 (50 sccm, standard cubic centimeter per minute) was used as a protective gas. For the selenization, the temperatures of selenium and the Pd film zone were increased to 200 °C and 357 °C, respectively. After 2 h of selenization, the color of Si/SiO_2 wafer changed slightly from navy to light gray.

B. characterization

The topography of as-selenized $PdSe_2$ nanofilm was examined by using an AFM (Benyuan Nanotech Com, CSPM-4000). The morphology of $PdSe_2$ was characterized by field-emission scanning electron microscopy (FESEM, SIRION 200 FEG) and energy-dispersive X-ray spectroscopy (EDS). The structure of $PdSe_2$ film was analyzed by an HR (Horiba Jobin Yvon) Raman spectrometer equipped with a 532 nm laser and X-ray diffractometer (Rigaku D/max-rB). The absorption spectra of the $PdSe_2$ film, the GaAs substrate and the $PdSe_2$/GaAs hybrid were recorded using a Shimadzu UV-2550 UV-Vis spectrophotometer.

C. Device fabrication and analysis

To construct the $PdSe_2$/GaAs heterojunction device, 50 nm gold was vaporized by electron beam evaporation on the back of n-type GaAs substrate (resistivity: $8 \times 10^{-4} - 9 \times 10^{-3}$ Ω·cm^{-1}) which was precleared by acetone, alcohol, and deionized water. Then a thin layer of PDMS was spin-coated onto the substrate as an insulating layer. After heating, a window was carved on PDMS by a tool knife as an effective area (0.2 cm×0.2 cm). A 5 wt% layer of polymethyl methacrylate (PMMA) was spin-coated on the $PdSe_2$ film, and then respectively immersed into NaOH solution (4 mol/L) and deionized water to remove the underlying SiO_2/Si and residual ions. Finally, the as-selenized $PdSe_2$ multiple layer was transferred onto the window. The electrical measurements of the $PdSe_2$/GaAs hybrid heterojunction were tested using a semiconductor characterization system (Keithley 2400). To further study the light response of the device, a number of NIR and UV laser diodes with different wavelengths (Thorlabs, M808L3, M970L3, M1300L3, M265L3 and M365L3) were employed. In order to measure the response speed, a signal generator (Tektronix, TDS2022B) was employed to drive the laser diode to produce pulsed irradiation with different frequencies, and an oscilloscope (Tektronix, TDS2012B) was used to record the electrical output. All tests were carried out at room temperature in ambient condition.

III. RESULTS AND DISCUSSION

The schematic geometry in FIG. 1(a) shows that the proposed device consists of the multilayered $PdSe_2$ film and an n-type GaAs wafer. The detailed device fabrication process is illustrated in FIG. S1(a) (supplementary materials). In short, 50 nm thick gold electrode was firstly coated on the backside of underlying GaAs by electron beam evaporation, and then a thin layer of polydimethylsiloxane (PDMS) was spin-coated as an insulating layer, followed by heating to solidify it. Afterwards, through a solution transfer method, multiple
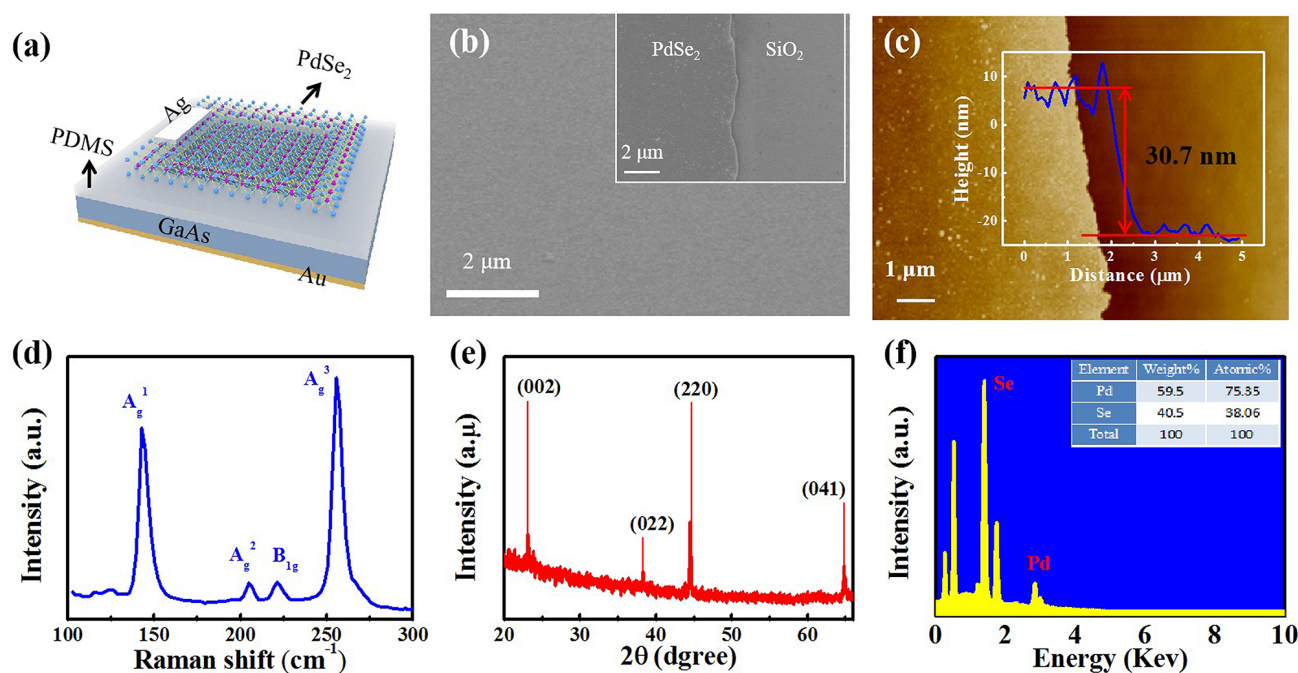
FIG. 1 (a) Schematic illustration of the PdSe$_2$/GaAs heterojunction photodetector. (b) FESEM image of PdSe$_2$ layer on a SiO$_2$/Si wafer, the inset shows the obvious contrast between PdSe$_2$ layer and SiO$_2$ substrate. (c) AFM image of the PdSe$_2$ film on the SiO$_2$/Si substrate, the inset shows the corresponding height profile. (d) Raman spectrum of the PdSe$_2$ film. (e) XRD pattern of PdSe$_2$ sample. (f) The corresponding EDS analysis of the PdSe$_2$ sample. For color image, see the online version.

layers of PdSe$_2$ that was prepared by a simple selenization process, were transferred at a pre-defined window. It can be clearly seen from FIG. S1(b) of supplementary materials that once Pd nanofilm is converted to PdSe$_2$ multilayer, the color will change from orchid to light gray. FIG. 1(b) displays a typical field emission scanning electron microscopy (FESEM) image of the PdSe$_2$ film. It is clear that the PdSe$_2$ sample has relatively continuous and smooth surface. The thickness of the as-selenized PdSe$_2$ film was estimated to be ∼30.7 nm, from the atomic force microscopy (AFM) image illustrated in FIG. 1(c). The Raman spectrum of the PdSe$_2$ nanofilm in FIG. 1(d) shows four distinct peaks, which are labeled as A$_g^1$, A$_g^2$, B$_{1g}$ and A$_g^3$, corresponding to ∼143.5, ∼206, ∼222, and ∼256 cm^{-1}, respectively [37]. Among these peaks, the three peaks with relatively low Raman shifts are associated with the motion mode of the Se atom, while the rest peak (A$_g^3$) should be ascribed to the relative motion between Se and Pd atoms. Further X-ray diffraction (XRD) study of the sample reveals a pentagonal structure with a=5.756 Å, b=5.874 Å, and c=7.698 Å, which are close to the values of standard card (PDF#11-0453). In fact, the chemical composition of the PdSe$_2$ was also confirmed by X-ray photoemission spectroscopy in FIG. S2 of supplementary materials, and the energy-dispersive X-ray spectroscopy (EDS) image in FIG. 1(f), according to which the ele-

mental ratio is determined to be Se:Pd≈1.98:1. Notably, both Se and Pd atoms are uniformly distributed on the whole PdSe$_2$ film (FIG. S3 (a) and (b) in supplementary materials). This result along with clear 2D lattice fringe image (FIG. S3 (c) in supplementary materials) suggests the good quality of the sample.

FIG. 2(a) depicts the current-voltage (I-V) characteristics of a PdSe$_2$/GaAs heterojunction device in the dark. Obviously, the device showed a typical one-way conduction behavior, with a relative low current ratio of ∼7 at ±2 V. Such a rectifying characteristic which has been observed in many other 2D based hybrid structures [38, 39] should stem from PdSe$_2$/GaAs interface in view of the fact that good contact was formed between Ag/PdSe$_2$/Ag and between Au/GaAs/Au (FIG. S4 in supplementary materials). It is easy to find in FIG. 2(b), when the hybrid structure was irradiated by 808 nm NIR light, obvious photovoltaic characteristics, with an open circuit (V_{oc}) of 0.51 V and short-circuit current (I_{sc}) of 4.05 μA was found. Even though the efficiency of energy conversion was rather low, this heterojunction device can function as a self-driven photodetector that is able to sense NIR illumination at 0 V bias. This photovoltaic characteristic can actually be interpreted by the energy band diagram in FIG. 2(c). Due to difference in work function (the work function of PdSe$_2$ multilayer is 5.49 eV, which is higher than that of n-
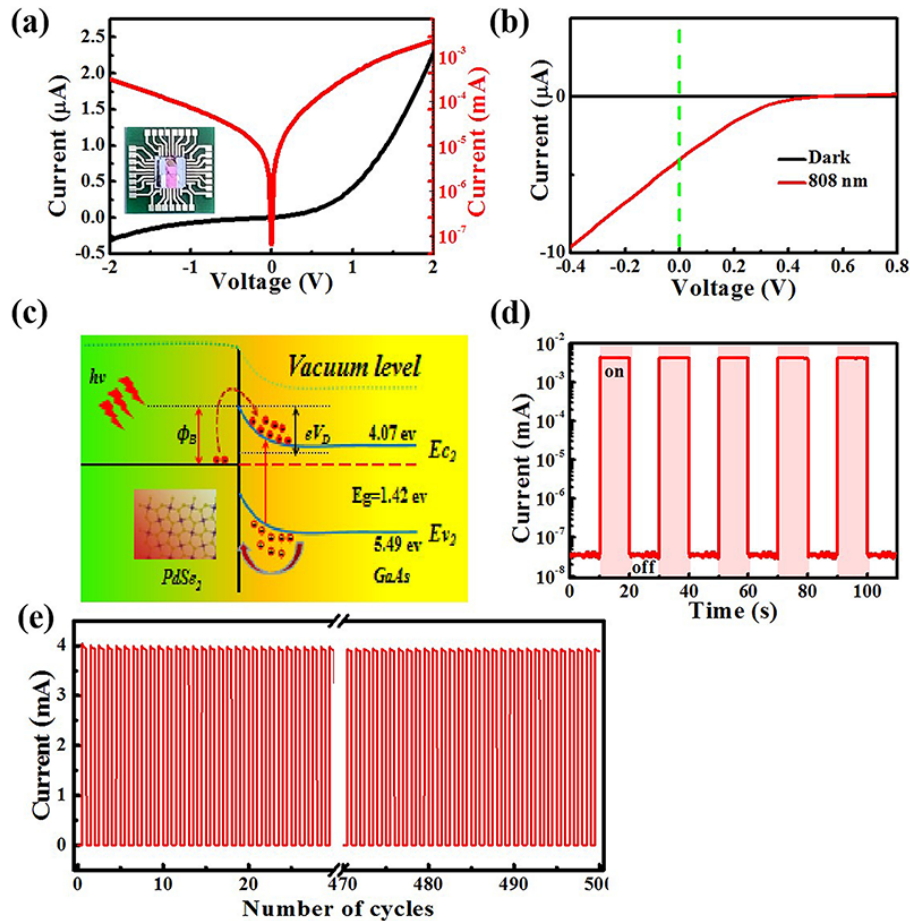
FIG. 2 (a) *I-V* curves of the PdSe$_2$/GaAs heterojunction device without light illumination, the inset shows a representative camera picture of the device. (b) *I-V* characteristics of the device in the dark and illuminated with 808 nm light (45.7 mW/cm^2). (c) Energy band diagram under illumination. (d) Switchable photoresponse of the device under 808 nm light illumination at zero bias. (e) Photoresponse of the device for about 500 cycles of operation. For color image, see the online version.

type GaAs), once the PdSe$_2$ is in contact with GaAs, the electrons will diffuse from GaAs to PdSe$_2$ while the holes diffuse from PdSe$_2$ to GaAs as the Fermi level of PdSe$_2$ is higher than GaAs. As a result, the energy levels near the GaAs surface will bend upwards, while PdSe$_2$ will bend downwards, forming a built-in electric field at the interface with a direction pointing from GaAs to PdSe$_2$. When irradiated by NIR light, the GaAs will absorb photons. It should be noted that the PdSe$_2$ acts as a transparent electrode, which means it will function like metal electrode, as observed in other conventional metal-semiconductor devices, in the meanwhile, it can also work as a graphene layer that can allow the incident light to penetrate into the underlying GaAs semiconductors. The electron-hole pairs generated at the interface were then separated by the built-in electric field, forming a photocurrent or photovoltage in the circuit [40]. FIG. 2(d) shows the time-dependent photoresponse with a bias voltage of 0 V at 808 nm (45.7 mW/cm^2). Clearly, our device was very sensitive to NIR light with good reproducibility even after hundreds

of cycles (FIG. 2(e)), the photocurrent/darkcurrent is estimated to be 1.16×10^5. In addition, steep rising and falling edges were also found, indicative of fast separation of photo-generated carriers in the depletion region.

Like most of other 2D materials based photodetectors, the photocurrent of the present device is found to strongly depend on the illumination intensity. As can be seen from the *I-V* and *I-t* at various intensities in FIG. 3(a, b), when the 808 nm NIR light intensity increases from 0.183 mW/cm^2 to 62.20 mW/cm^2, the photocurrent will gradually increase accordingly. Besides, the photovoltage displays similar trend. It is reasonable for that the number of photo-generated carriers excited at higher light intensities have increased (FIG. 3(c)). However, when the light intensity reached a certain value (about 9 mW/cm^2), both photovoltage and $I_{\text{light}}/I_{\text{dark}}$ began to saturate, irrespective of the further increase in light intensity. For better understanding the relationship between the dependence of photocurrent and light intensity, the photoresponse of the device under different light intensities was then studied. As plot-
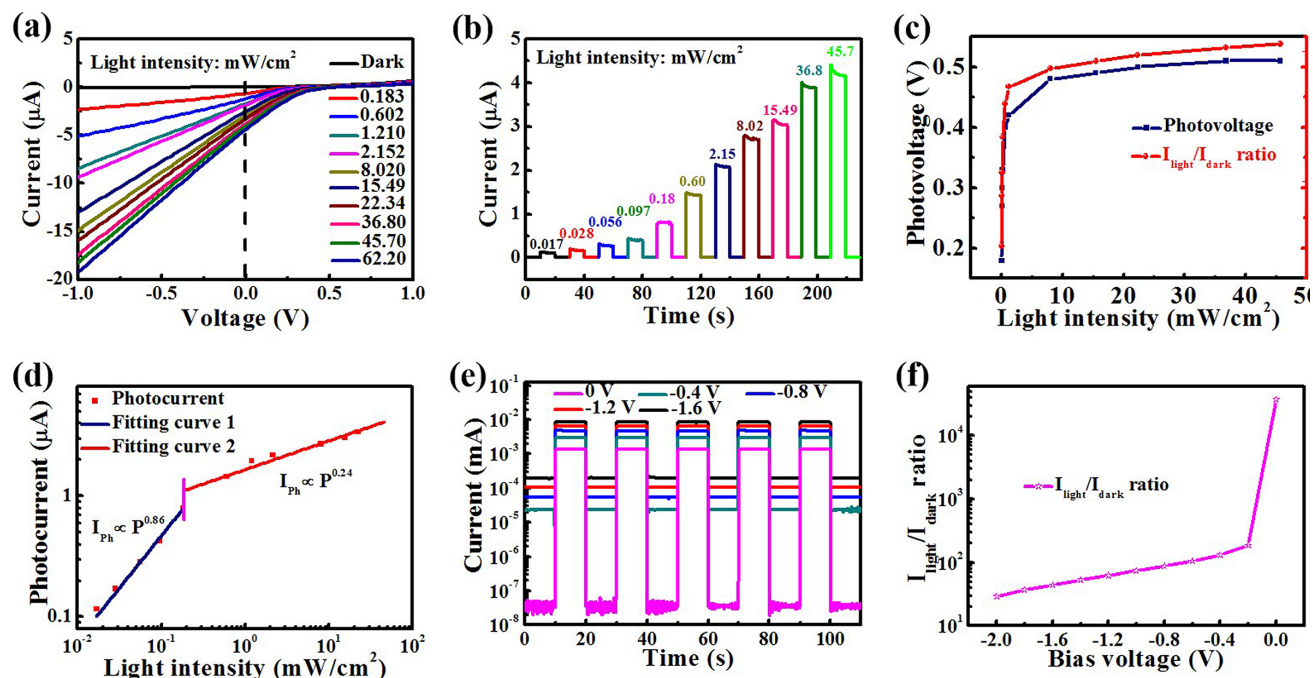
FIG. 3 (a) *I-V* curves of the heterojunction device under 808 nm light with different intensities. (b) Photoresponse of the heterojunction device under 808 nm light with different intensities. (c) The dependence of photovoltage and I_{light}/I_{dark} ratio on light intensity. (d) Corresponding fitting curve of the photosensing behavior with various incident light intensities. (e) Repeated photoresponse of the device at zero and different reverse bias voltages. (f) I_{light}/I_{dark} ratio of the device as a function of different bias voltages. For color image, see the online version.

ted in FIG. 3(d), their relationship can be numerically described by the power law $I_{ph} \propto P^{\theta}$, where I_{ph} is the current with light illumination, P is the light intensity, and θ is the response index of the photocurrent to the NIR light. For sake of convenience, the light intensity range is divided into two parts, the weak intensity ranges from 16.92 µW/cm^2 to 182.5 µW/cm^2 and the strong intensity ranges from 0.602 mW/cm^2 to 22.34 mW/cm^2. Fitting the experiment result will obtain two θ values, which are θ=0.86 in the weak intensity region; and θ=0.24 in the high intensity region and due to the recombination loss, the deviation of these two fitted values from the ideal value θ=1 was reasonable. On the other hand, it is also observed in FIG. 3(e) that both dark current and photocurrent were determined by the bias voltage as well. In order to unveil how the bias voltage affected the photoelectric property of the hybrid structure device, the I_{light}/I_{dark} at different bias voltages was examined. As can be seen from FIG. 3(f), with the increase of the negative bias, the I_{light}/I_{dark} ratio gradually decreased, and the maximum value at 0 V was $I_{light}/I_{dark} \approx 0.37 \times 10^5$, the minimum value at -2 V was $I_{light}/I_{dark} \approx 29$. This is because the dark current increased at a rate which was faster than that of the photocurrent as the bias voltage increased at the same light intensity [36].

For quantitative evaluation of the photoresponse of the PdSe$_2$/GaAs heterojunction device to 808 nm NIR

light, the following two formulas are used to calculate both R and external quantum efficiency (EQE) [41, 42]. The R represents the responsivity, which can be calculated by the photocurrent (I_{light}), dark current (I_{dark}), light intensity (P), and effective area (S) in Eq.(1):

$$R = \frac{I_{light} - I_{dark}}{PS} \tag{1}$$

EQE represents the number of effective carriers formed by each NIR photon, which can be described by Eq.(2):

$$EQE = \frac{Rhc}{e\lambda} \tag{2}$$

Where h, c, e, and λ are the Planck constant, the speed of light, the elementary charge, and the incident wavelength, respectively. FIG. 4 (a) and (b) summarize the responsivity and EQE under a variety of light intensities. Obviously, both parameters decrease substantially with the increase of light intensity. Specifically, when the light intensity is as weak as 16.92 µW/cm^2, the responsivity and EQE reach the highest value, which are 171.34 mA/W and 26.3%, respectively (Please see the supplementary materials for detailed information about the calculation). In addition to responsivity, the photodetector has another important performance metric, the specific detectivity (D^*). Such parameter is usually used to measure the capability of NIRPD to detect weak optical signals from noise, which can be calculated
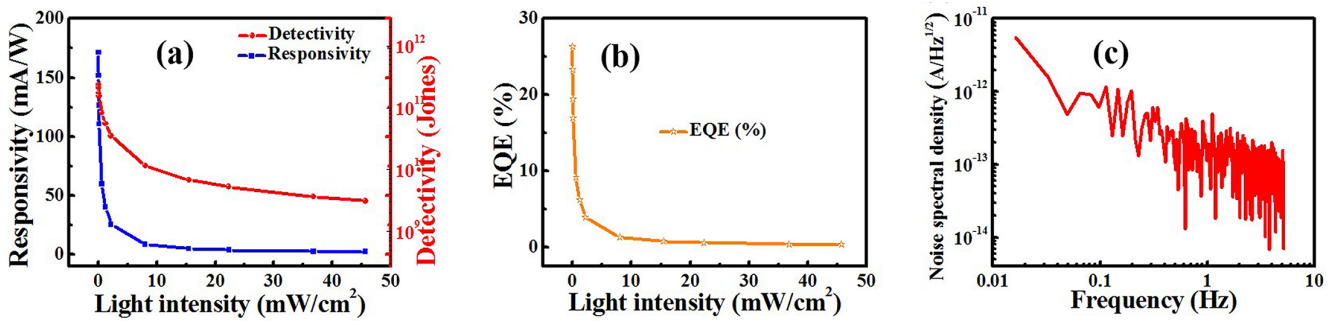
FIG. 4 (a) Calculated responsivity and detectivity as a function of the. (b) The EQE of the PdSe$_2$/GaAs heterojunction under 808 nm light with varied light intensities at zero bias. (c) Analysis of noise spectral density of the device with the dark current noise using Fourier transform. For color image, see the online version.

by using noise equivalent power from the following two formulas [43, 44].

$$D^* = \frac{(S\Delta f)^{1/2}}{NEP} \quad (3)$$

$$\mathrm{NEP} = \frac{\overline{i_n{}^2}^{1/2}}{R} \quad (4)$$

where S, Δf, and $\overline{i_n{}^2}^{1/2}$ represent the effective area (0.04 cm^2), bandwidth, and root mean square value of the noise current of the hybrid structure device, respectively. As described by FIG. 4(c), the $\overline{i_n{}^2}^{1/2}$ was obtained by locking the hybrid structure device equipped with a preamplifier in dark condition for recording its noise current at different frequencies [45]. The noise level of $\overline{i_n{}^2}^{1/2}$ was determined at the frequency of 1 Hz, which is approximately 1.45×10^{-13} A·Hz$^{-1/2}$ in this work. FIG. 4(a) shows the trend of the specific detectivity as a function of light intensity. Obviously, when the weak light intensity was 16.92 µW/cm^2, the maximum specific detectivity was as high as 2.36×10^{11} Jones.

Next, the changes of both responsivity and specific detectivity of the PdSe$_2$/GaAs device at different wavelengths were investigated. FIG. 5(a) displays the continuous spectral response in the range of 200 nm to 1200 nm. It is apparent that device has a very good spectral selectivity, with peak response at around 800 nm, for which 808 nm light emitting diodes (LED) were chosen as the light source in the device performance characterization. Such a difference in spectral selectivity is in good consistence with the absorption spectrum. FIG. 5(b) plots the absorption spectra of pure GaAs wafer, pure PdSe$_2$ and multilayer PdSe$_2$ on GaAs wafer. One can easily observe that the absorption curve of the hybrid structure is mainly at around 800 nm. Although the hybrid structure also absorbs UV and other NIR light longer than 900 nm, the absorption is rather weak, which can explain why the responsivity and specific detectivity are smaller in both UV and NIR region. Apart from the pronounced photoresponse to 800 nm NIR illumination, the present NIRPD exhibits weak

but repeatable photoresponse to irradiation of ultraviolet C(UVC), ultraviolet A(UVA) and NIR illumination with wavelength longer than 808 nm. FIG. 5 (c−e) plot the main photoresponse parameters irradiated by 265, 365 and 970 nm light. The PdSe$_2$/GaAs heterojunction device can be readily switched between high- and low-conduction states. In comparison, the photocurrent under 265 nm was relatively higher than that under 365 and 970 nm. Remarkably, for all the three different illuminations, the $I_{\mathrm{light}}/I_{\mathrm{dark}}$ ratio of NIRPD gradually increases with increasing light intensity (FIG. 5(d)). It is also interesting to find that the present NIRPD is even sensitive to NIR illumination with wavelength of 1300 nm, although the response current was on the scale of nA, as shown in FIG. 5(f).

The response speed is a typical parameter that reflects the ability of a photodetector to catch a fast varying optical signal [46, 47]. In this work, the as-fabricated PdSe$_2$/GaAs heterojunction device can detect high-frequency optical pulse with good reproducibility. For studying the response speed, an experiment setup that is composed of a digital oscilloscope used to record temporal photoresponse signal (photovoltaic changes with time) when switching frequency ranging from 200 Hz to 5 kHz was then employed (FIG. 6(a)). FIG. 6 (b−d) depict the photoresponse of the hybrid heterojunction device to pulsed illumination at different frequencies. Obviously, the NIRPD can be repeatedly switched between on- and off-states, even the frequency is as high as 4 kHz. The response rate of device can be determined from an individual cycle of the responsive curve in FIG. 6(e). In the time domain, the rise and fall time that is required for the current to increase from 10% to 90% of the peak value (and vice versa) can directly determine the speed of the photodetector [48]. According to the above definition, the rise time and fall time of our devices were 43.76 and 89.98 µs, respectively. Furthermore, the relative balance $(V_{\mathrm{max}}-V_{\mathrm{min}})/V_{\mathrm{max}}$ of the photovoltage as a function of frequency was calculated and plotted in FIG. 6(f), from which the f_{3db} bandwidth(the frequencies when $(V_{\mathrm{max}}-V_{\mathrm{min}})/V_{\mathrm{max}}=70\%$) is estimated to be ∼50 Hz [49]. The main parameters including R, D^*,
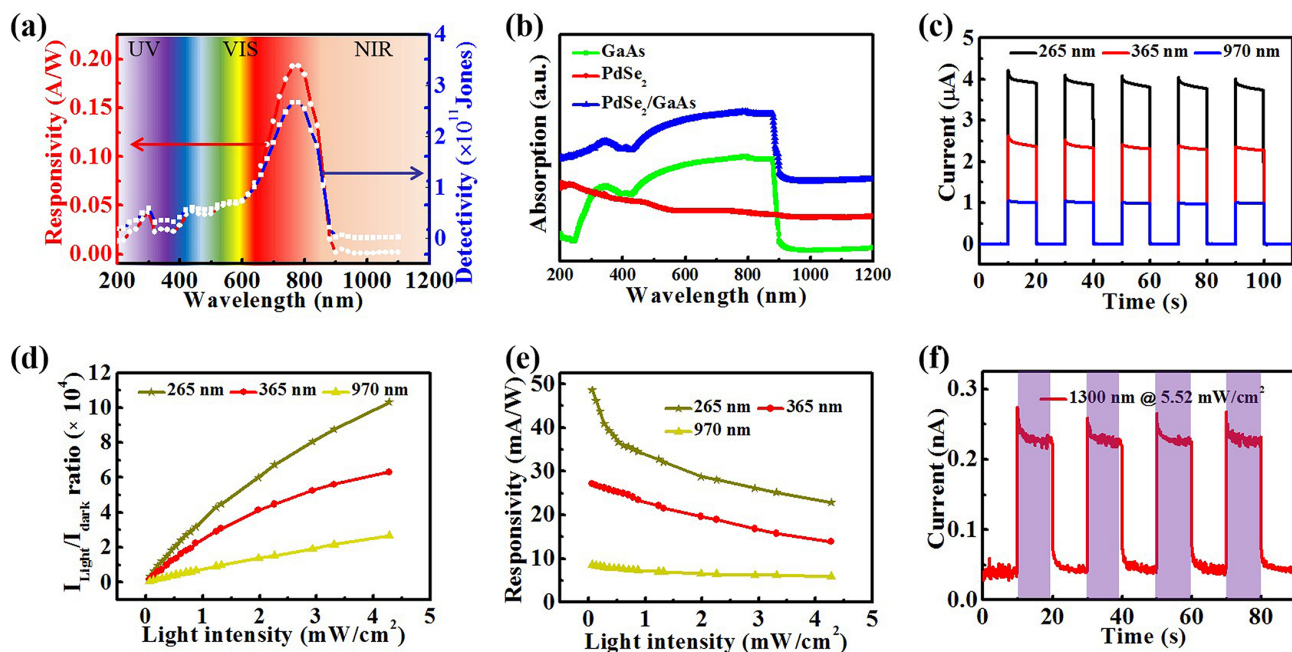
FIG. 5 (a) Wavelength-dependent responsivity and detectivity of the PdSe$_2$/GaAs device. (b) Absorption spectrum of the PdSe$_2$ nanofilm, GaAs substrate, and PdSe$_2$/GaAs hybrid structure. (c) Time-dependent photoresponse of the device under illumination of different light sources (4.28 mW/cm^2) at zero bias. (d) $I_{\text{light}}/I_{\text{dark}}$ ratios as a function of the light intensity for different wavelengths. (e) The relationship between the responsivity and the light intensity for 265, 365, 970 nm. (f) Photoresponse of the device under 1300 nm light illumination (5.52 mW/cm^2) at zero bias. For color image, see the online version.
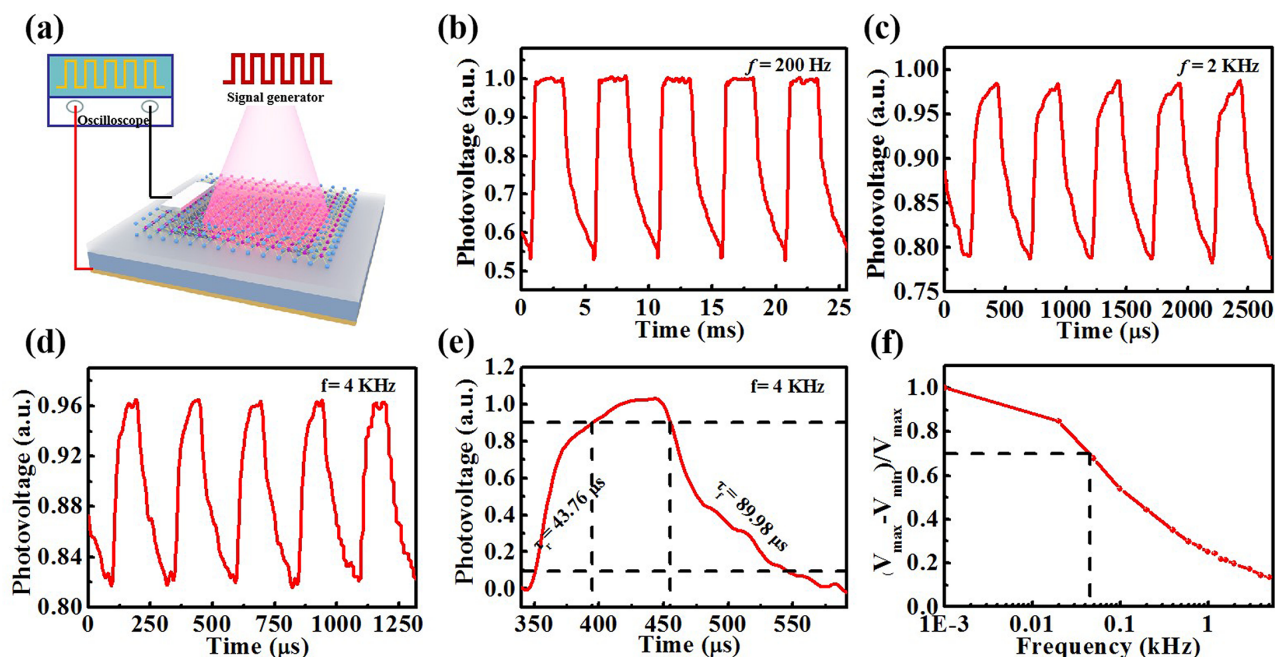

FIG. 6 (a) The experiment setup for studying the photoresponse of the heterojunction device. Photoresponse of the device under pulsed light irradiation (808 nm) with a frequency of 200 Hz (b), 2 kHz (c), and 4 kHz (d), respectively. (e) A single normalized cycle measured at the frequency of 4 kHz to calculate both rise time (τ_{r}) and fall time (τ_{f}). (f) The relative balance ($V_{\text{max}}-V_{\text{min}}$)/$V_{\text{max}}$ versus switching frequency, the 3 dB cutoff frequency is estimated to be ~50 Hz. For color image, see the online version.

TABLE I Summary of some of the key parameters of the PdSe$_2$/GaAs photodetector and other similar devices.

| Device structure	R/A·W^{-1}	D^*/Jones	I_{light}/I_{dark} ratio	τ_r/τ_f	Wavelength/nm	Reference
PdSe$_2$/GaAs	0.171	2.36×10^{11}	1.16×10^5	43.76/89.98	808 (V=0 V)	Our work
PdSe$_2$/pyramid Si	0.456	9.97×10^{13}	1.6×10^5	14.1/15.9	980 (V=0 V)	[36]
PdSe$_2$/MoS$_2$	0.186	8.21×10^9	–	65.3/62.4	10600 (V=1 V)	[37]
MoS$_2$/GaAs	0.035	1.96×10^{13}	6.6×10^3	3.4/15.6	780 (V=0 V)	[39]
UCNPs/Gra/GaAs	0.006	1.1×10^{11}	1.17×10^4	–	980 (V=0 V)	[38]
Gra/Ge	0.052	1.38×10^{10}	2×10^4	23/108	1550 (V=0 V)	[44]
Gra/Si	0.029	3.9×10^{11}	102	93/110	850 (V=0 V)	[25]
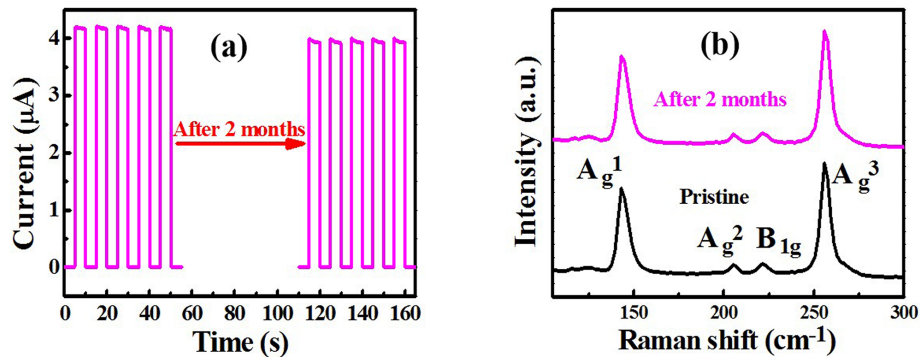
FIG. 7 (a) Comparison of the photoresponse of the NIRPD with and without 2 months' storage in air. (b) Comparison of the Raman spectra of the PdSe$_2$ before and after two months. For color image, see the online version.
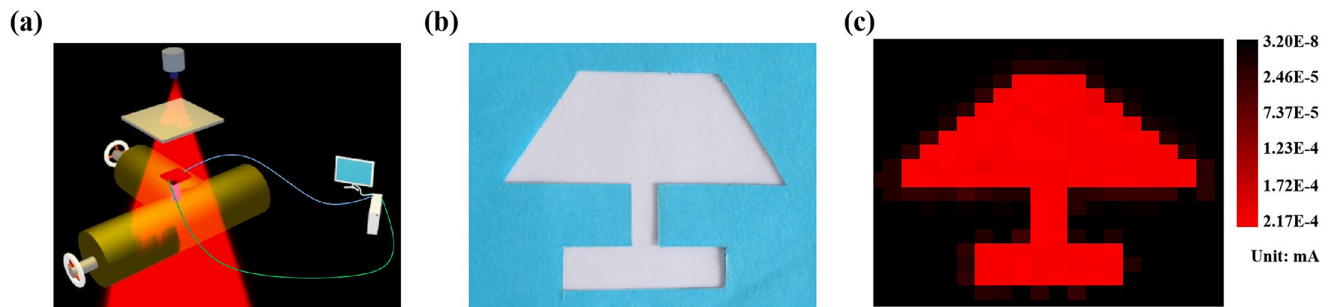
FIG. 8 (a) Schematic illustration of the setup for the NIR image sensing application. (b) Digital photograph of the template "table lamp". (c) The corresponding 2D current mapping of image "table lamp" under 808 nm illumination. For color image, see the online version.

I_{light}/I_{dark} ratio, τ_r/τ_f of the present NIRPD and other similar devices are compared in Table I. It can be clearly seen that although the I_{light}/I_{dark} ratio is slightly lower than that of PdSe$_2$/pyramid Si heterojunction device, the I_{light}/I_{dark} ratio of the present NIRPD is at least an order of magnitude higher than that of other geometies. In addition, the responsivity and specific detectivity are higher than most of the device included in the Table I.

The above results have demonstrated that the present PdSe$_2$/GaAs exhibits good responsivity to NIR illumination. However, from the perspective of practical application, another issue regarding to the long-term stability is also very important and deserves further study. In order to check the stability of the PdSe$_2$/GaAs het-

erojunction devices in ambient condition, we compared the devices performance in air for two months without any encapsulation. It was worth noting that the device can almost retain its photoresponse, and no obvious degradation in photocurrent was observed. The high stability of the device is without doubt due to the good stability of PdSe$_2$ and GaAs in air, as verified by the Raman analysis of multilayered PdSe$_2$ in FIG. 7(b).

As an important optoelectronic device, infrared image sensor has been widely used in night vision, missile warning system, video and biomedical imaging, and even fire monitoring, *etc.* [50, 51]. By utilizing the setup illustrated in FIG. 8(a), the capability of the present photodetector for NIR imaging was then explored. For

the sake of mapping the photocurrent, the NIRPD was mounted on an automatic placement system below, and a simple "table lamp" pattern as shown in FIG. 8(b) was illuminated vertically with an 808 nm LED source. Then, a computer pre-installed with customized software will help manipulate the detector to scan horizontally (X-axis) and vertically (Y-axis) at a step of 1 mm. During the image scanning process, the channel current of each pixel was measured and recorded, and then incorporated into a 2D contrast mapping system. FIG. 8(c) shows the image sensing results in the 2D contrast mapping system. Obviously, the position where the NIR light can transmit shows relatively high photocurrent while the blocked area displays low current, leading to the formation of NIR profile of "table lamp" pattern. Although there are some glitches at the edges of the picture, the pattern of the table lamp can be clearly distinguished from the background. Such a relatively good imaging quality indicates that the present hybrid heterojunction based NIRPD may find potential applications in future NIR optoelectronic and image sensing systems.

IV. CONCLUSION

In summary, we have developed a high sensitive hybrid heterojunction NIRPD by simply transferring PdSe$_2$ thin film onto a GaAs wafer. The as-fabricated device exhibited obvious photovoltaic behavior under 808 nm light, which indicates that the device can be used as a self-driven NIRPD without external power supply. Further analysis reveals that the device was very sensitive to 808 nm NIR illumination at zero bias voltage, with excellent reproducibility, ambient stability and an $I_{\text{light}}/I_{\text{dark}}$ ratio as high as 1.16×10^5, which was higher than most of other Pt/Pd chalcogenides photodetectors ever reported. Specifically, the responsivity and specific detectivity of the device were estimated to be 171.34 mA/W and 2.36×10^{11} Jones, respectively. Finally, the PdSe$_2$/GaAs-based heterojunction device can easily record an NIR "table lamp" image generated by 808 nm illumination, suggesting the potential application of the present device in future infrared optoelectronic systems.

V. ACKNOWLEDGMENTS

[1] J. H. Li, L. Y. Niu, Z. J. Zheng, and F. Yan, Adv. Mater. **26**, 5239 (2014).

[2] T. Mueller, F. N. Xia, and P. Avouris, Nat. Photonics **4**, 297 (2010).

[3] F. H. L. Koppens, T. Mueller, P. Avouris, A. C. Ferrari, M. S. Vitiello, and M. Polini, Nat. Nanotechnol. **9**, 780 (2014).

[4] F. X. Liang, J. Z. Wang, Z. P. Li, and L. B. Luo, Adv. Opt. Mater. **5**, 1700081 (2017).

[5] J. S. Miao, W. D. Hu, N. Guo, Z. Y. Lu, X. M. Zou, L. Liao, S. X. Shi, P. P. Chen, Z. Y. Fan, J. C. Ho, T. X. Li, X. S. Chen, and W. Lu, ACS Nano **8**, 3628 (2014).

[6] D. S. Zheng, H. H. Fang, M. S. Long, F. Wu, P. Wang, F. Gong, X. Wu, J. C. Ho, L. Liao, and W. D. Hu, ACS Nano **12**, 7239 (2018).

[7] M. Rezaei, M. S. Park, C. Rabinowitz, C. L. Tan, S. Wheaton, M. Ulmer, and H. Mohseni, Appl. Phys. Lett. **114**, 161101 (2019).

[8] M. Horstmann, M. Marso, A. Fox, F. Rüders, M. Hollfelder, H. Hardtdegen, P. Kordos, and H. Lüth, Appl. Phys. Lett. **67**, 106 (1995).

[9] M. Piccardo, N. A. Rubin, L. Meadowcroft, P. Chevalier, H. Yuan, J. Kimchi, and F. Capasso, Appl. Phys. Lett. **112**, 041106 (2018).

[10] R. Avrahamy, M. Zohar, M. Auslender, Z. Fradkin, B. Milgrom, R. Shikler, and S. Hava, Appl. Opt. **58**, F1 (2019).

[11] J. Y. Zhou, M. A. Raihan Miah, Y. G. Yu, A. C. Zhang, Z. J. Zeng, S. Damle, I. A. Niaz, Y. Zhang, and Y. H. Lo, Opt. Express **27**, 37056 (2019).

[12] N. Killilea, M. J. Wu, M. Sytnyk, A. A. Yousefi Amin, O. Mashkov, E. Spiecker, and W. Heiss, Adv. Funct. Mater. **29**, 1807964 (2019).

[13] J. C. Tong, F. Suo, W. Zhou, Y. Qu, N. J. Yao, T. Hu, Z. M. Huang, and D. H. Zhang, Opt. Express **27**, 30763 (2019).

[14] B. Das, N. S. Das, S. Sarkar, B. K. Chatterjee, and K. K. Chattopadhyay, ACS Appl. Mater. Interfaces **9**, 22788 (2017).

[15] L. He, J. R. Yang, S. L. Wang, Y. Wu, and W. Z. Fang, Adv. Mater. **11**, 1115 (1999).

[16] D. C. Elias, I. Shafir, T. Meir, O. Sinai, D. Memram, S. S. Shusterman, and M. Katz, Infrared Phys. Technol. **95**, 199 (2018).

[17] C. Wang, T. Hu, and E. J. Kan, Chin. J. Chem. Phys. **32**, 327 (2019).

[18] R. Nashed, C. Pan, K. Brenner, and A. Naeemi, IEEE J. Electron Devices Soc. **4**, 466 (2016).

[19] L. Tao, H. Li, M. X. Sun, D. Xie, X. M. Li, and J. B. Xu, IEEE Electron Device Lett. **39**, 987 (2018).

[20] D. H. Zhang, J. Zhou, C. L. Liu, S. K. Guo, J. N. Deng, Q. Y. Cai, Z. F. Li, Y. F. Zhang, W. Q. Zhang, and X. S. Chen, J. Appl. Phys. **126**, 074301 (2019).

[21] S. Rumyantsev, G. X. Liu, M. S. Shur, R. A. Potyrailo, and A. A. Balandin, Nano Lett. **12**, 2294 (2012).

[22] X. M. Wang, S. G. Wu, H. Liu, L. Zhou, and Q. P. Zhao, Chin. J. Chem. Phys. **26**, 590 (2013).

[23] X. M. Wang, Z. Z. Cheng, K. Xu, H. K. Tsang, and J. B. Xu, Nat. Photonics **7**, 888 (2013).

[24] F. Yang, H. Cong, K. Yu, L. Zhou, N. Wang, Z. Liu, C. B. Li, Q. M. Wang, and B. W. Cheng, ACS Appl. Mater. Interfaces **9**, 13422 (2017).

[25] P. Lv, X. J. Zhang, X. W. Zhang, W. Deng, and J. S. Jie, IEEE Electron Device Lett. **34**, 1337 (2013).

[26] L. B. Luo, H. Hu, X. H. Wang, R. Lu, Y. F. Zou, Y. Q. Yu, and F. X. Liang, J. Mater. Chem. C **3**, 4723 (2015).

[27] Y. R. Lim, W. Song, J. K. Han, Y. B. Lee, S. J. Kim, S. Myung, S. S. Lee, K. S. An, C. J. Choi, and J. Lim, Adv. Mater. **28**, 5025 (2016).

[28] A. S. Aji, P. S. Fernandez, H. G. Ji, K. Fukuda, and H. Ago, Adv. Funct. Mater. **27**, 1703448 (2017).

[29] V. Dhyani, M. Das, W. Uddin, P. K. Muduli, and S. Das, Appl. Phys. Lett. **114**, 121101 (2019).

[30] I. G. Lezama, A. Arora, A. Ubaldini, C. Barreteau, E. Giannini, M. Potemski, and A. F. Morpurgo, Nano Lett. **15**, 2336 (2015).

[31] A. N. Hoffman, Y. Y. Gu, L. B. Liang, J. D. Fowlkes, K. Xiao, and P. D. Rack, NPJ 2D Mater. Applicat. **3**, 1 (2019)

[32] S. H. Zhang and B. G. Liu, J. Mater. Chem. C **6**, 6792 (2018).

[33] D. Wu, J. W. Guo, J. Du, C. X. Xia, L. H. Zeng, Y. Z. Tian, Z. F. Shi, Y. T. Tian, X. J. Li, Y. H. Tsang, and J. S. Jie, ACS Nano **13**, 9907 (2019).

[34] L. H. Zeng, D. Wu, S. H. Lin, C. Xie, H. Y. Yuan, W. Lu, S. P. Lau, Y. Chai, L. B. Luo, Z. J. Li, and Y. H. Tsang, Adv. Funct. Mater. **29**, 1806878 (2019).

[35] Q. J. Liang, Q. X. Wang, Q. Zhang, J. X. Wei, S. X. D. Lim, R. Zhu, J. X. Hu, W. Wei, C. K. Lee, C. H. Sow, W. J. Zhang, and A. T. S. Wee, Adv. Mater. **31**, e1807609 (2019).

[36] F. X. Liang, X. Y. Zhao, J. J. Jiang, J. G. Hu, W. Q. Xie, J. Lv, Z. X. Zhang, D. Wu, and L. B. Luo, Small **15**, 1903831 (2019).

[37] M. S. Long, Y. Wang, P. Wang, X. H. Zhou, H. Xia, C. Luo, S. Y. Huang, G. W. Zhang, H. G. Yan, Z. Y. Fan,

X. Wu, X. S. Chen, W. Lu, and W. D. Hu, ACS Nano **13**, 2511 (2019).

[38] J. H. Wu, Z. W. Yang, C. Y. Qiu, Y. J. Zhang, Z. Q. Wu, J. Z. Yang, Y. H. Lu, J. F. Li, D. X. Yang, R. Hao, E. P. Li, G. L. Yu, and S. S. Lin, Nanoscale **10**, 8023 (2018).

[39] C. Jia, D. Wu, E. P. Wu, J. W. Guo, Z. H. Zhao, Z. F. Shi, T. T. Xu, X. W. Huang, Y. T. Tian, and X. J. Li, J. Mater. Chem. C **7**, 3817 (2019).

[40] Q. S. Lv, F. G. Yan, X. Wei, and K. Y. Wang, Adv. Opt. Mater. **6**, 1700490 (2018).

[41] W. W. Tang, C. L. Liu, L. Wang, X. S. Chen, M. Luo, W. L. Guo, S. W. Wang, and W. Lu, Appl. Phys. Lett. **111**, 153502 (2017).

[42] C. Y. Zhang, S. Wang, L. J. Yang, Y. Liu, T. T. Xu, Z. Y. Ning, A. Zak, Z. Y. Zhang, R. Tenne, and Q. Chen, Appl. Phys. Lett. **100**, 243101 (2012).

[43] Y. Y. Wang, Y. D. Wu, W. Peng, Y. H. Song, B. Wang, C. Y. Wu, and Y. Lu, Nanoscale **10**, 18502 (2018).

[44] L. H. Zeng, M. Z. Wang, H. Hu, B. Nie, Y. Q. Yu, C. Y. Wu, L. Wang, J. G. Hu, C. Xie, F. X. Liang, and L. B. Luo, ACS Appl. Mater. Interfaces **5**, 9362 (2013).

[45] W. Deng, L. M. Huang, X. Z. Xu, X. J. Zhang, X. C. Jin, S. T. Lee, and J. S. Jie, Nano Lett. **17**, 2482 (2017).

[46] J. Mao, Y. Q. Yu, L. Wang, X. J. Zhang, Y. M. Wang, Z. B. Shao, and J. S. Jie, Adv. Sci. **3**, 1600018 (2016).

[47] X. F. Wang, H. M. Zhao, S. H. Shen, Y. Pang, P. Z. Shao, Y. T. Li, N. Q. Deng, Y. X. Li, Y. Yang, and T. L. Ren, Appl. Phys. Lett. **109**, 201904 (2016).

[48] B. Nie, J. G. Hu, L. B. Luo, C. Xie, L. H. Zeng, P. Lv, F. Z. Li, J. S. Jie, M. Feng, C. Y. Wu, Y. Q. Yu, and S. H. Yu, Small **9**, 2872 (2013).

[49] J. C. Carrano, D. L. Brown, P. A. Grudowski, C. J. Eiting, R. D. Dupuis, and J. C. Campbell, Appl. Phys. Lett. **73**, 2405 (1998).

[50] Z. H. Sun, Z. K. Liu, J. H. Li, G. A. Tai, S. P. Lau, and F. Yan, Adv. Mater. **24**, 5878 (2012).

[51] A. Rogalski, J. Antoszewski, and L. Faraone, J. Appl. Phys. **105**, 091101 (2009).